

# Chip-Scale Quadrupole Mass Filters for Portable Mass Spectrometry

Kerry Cheung, *Member, IEEE*, Luis Fernando Velásquez-García, *Member, IEEE*, and Akintunde Ibitayo Akinwande, *Fellow, IEEE*

**Abstract**—We report the design, fabrication, and characterization of a new class of chip-scale quadrupole mass filter (QMF). The devices are completely batch fabricated using a wafer-scale process that integrates the quadrupole electrodes, ion optics, and housing into a single monolithic block. This process eliminates the electrode-to-housing misalignments inherent in other QMFs and enables the implementation of complex device architectures. To achieve the reported integration,  $1\text{ mm} \times 1\text{ mm}$  square electrodes of heavily doped silicon were utilized, resulting in quadrupoles with an effective aperture radius of  $0.707\text{ mm}$  and a length of  $30\text{ mm}$ . Mass filtering was demonstrated with this unconventional device showing a mass range of  $650\text{ amu}$  and a resolution of  $\sim 30$  at a drive frequency of  $1.8\text{ MHz}$ . When operated in the second stability region at  $2.0\text{ MHz}$  and a mass range of  $50\text{ amu}$ , a peak width of  $0.3\text{ amu}$  was achieved at mass 28, showing a resolution of  $\sim 90$ . This paper introduces operation in the second stability region as a reliable method for turning QMFs with less than ideal electrode geometries into high-performance devices. [2009-0325]

**Index Terms**—Chip-scale quadrupole, mass filter, second stability region, square electrodes.

## I. INTRODUCTION

MASS spectrometers are powerful analytical instruments that have a wide range of applications spanning national security, environmental monitoring, space exploration, industrial processing, healthcare, and many others. In recent years, there has been a growing desire to take these useful tools into space and into the field to perform analyses in harsh environments. To achieve this migration, mass spectrometers need to be small, light, mechanically and thermally robust, and low powered. Miniaturization addresses most of these requirements by achieving portability from the reduction of size and weight. Additionally, the smaller devices will enable operation at higher pressures, relaxing the need for large, heavy, and power-hungry vacuum pumps [1]–[4].

The four major components of a mass spectrometer are the ionizer, the mass analyzer, the detector, and the vacuum pump.

Manuscript received December 18, 2009; revised March 4, 2010. This work was supported in part by the Defense Advanced Research Projects Agency (DARPA)/Microsystems Technology Office and in part by the U.S. Army Soldier Systems Center, Natick, MA, under Contract W911QY-05-1-0002 (DARPA program managers C. Nguyen and D. Polla and Army program manager H. Girolamo). Subject Editor R. R. A. Syms.

The authors are with the Microsystems Technology Laboratories, Massachusetts Institute of Technology, Cambridge, MA 02139 USA (e-mail: cheung@mit.edu).

Color versions of one or more of the figures in this paper are available online at <http://ieeexplore.ieee.org>.

Digital Object Identifier 10.1109/JMEMS.2010.2046396

The ionizer places a charge on the compound to be analyzed, the mass analyzer sorts these ions according to their mass-to-charge ratios ( $m/e$  or  $m/z$ ), the detector counts the number of ions that make it through the mass analyzer, and the pump keeps the system at a pressure level at which the other parts can properly operate. These components have all been scaled down in one form or another by using conventional machining technologies. In particular, the mass analyzer has been the focus of numerous miniaturization efforts. Many researchers have focused on scaling down the Paul ion trap [5], [6], the cylindrical ion trap (CIT) [7]–[10], the quadrupole [11]–[16], the time-of-flight (TOF) [17]–[19], and the magnetic sector instruments [20], [21]. There has also been interesting developments with toroidal ion traps [22], halo ion traps [23], [24], rectilinear ion traps (RITs) [25], [26], and even fully functional systems [27]–[30]. Despite the good performance achieved with these instruments, the machining methodology is relatively expensive, and it serves to limit the adoption of these useful tools.

Microelectromechanical systems (MEMS) technology is another method for miniaturizing the mass spectrometer [31], [32]. The economies of scale from microfabrication can lead to lowered costs, while the associated micrometer-to-submicrometer precision and potential for component integration holds the promise of high-performance devices. In some cases, the highly repeatable nature of completely batch-fabricated devices would provide additional cost savings since each component will not require individual characterization. These benefits can greatly expand the utility of mass spectrometers, enabling light-weight, affordable, and versatile chemical sensors that will drive the development of many new applications. If these systems are sufficiently low-cost, chip-scale mass spectrometers will become a commodity item.

Ionizers [33], [34] and detectors [35], [36] have been developed with MEMS technology, but the mass analyzer has undergone the most research and development. Microfabricated cross-field [37], TOF [38], [39], CIT [40]–[42], ion mobility [43], [44], and traveling wave mass analyzers [45], [46] have all been implemented to date. There has also been substantial work on the popular quadrupole mass filter (QMF). This type of mass analyzer is extremely versatile due to its electronically controlled performance. It is possible to alter the mass range, the transmission, and the resolution by simply changing the drive signals applied to the device [47], [48]. The work on MEMS-based quadrupoles has been quite successful beginning with Taylor's gold-coated optical fibers that were soldered to V-grooves etched into silicon [49], [50]. Microsaic Systems Ltd. (U.K.) implemented devices using silicon deflection springs

to hold and align metallic cylindrical electrodes that have produced impressive results [51], [52]. Velásquez-García *et al.* also utilized silicon deflection springs but in a 3-D packaging scheme that facilitated the alignment and assembly of stainless steel electrodes to form out-of-plane quadrupoles [53].

In spite of their performance, the MEMS-based QMFs mentioned all require postfabrication electrode assembly that can lead to electrode-to-housing misalignments and increased costs. Misalignments limit the maximum performance achievable with a QMF [48], and the serial assembly needed for these devices place a bottleneck on mass production. Conversely, quadrupoles with hyperbolic electrodes made by LIGA (a German acronym for lithography, electroplating, and molding) [54] and very small devices made from semiconducting cantilevers [55] demonstrated complete batch-fabrication, but no experimental data were presented. Sillon and Baptist also mentioned a batch-fabricated QMF with square rods but no designs, device fabrication, or data were included [37]. Another limitation of the reported silicon-based QMFs is their robustness in harsh environments where high temperatures and vibrations are a concern. The solder in Taylor's device will melt at elevated temperatures, whereas the devices using silicon deflection springs will have a high likelihood of shifted or dislodged electrodes under intense vibrations.

In this paper, we present a chip-scale QMF that addresses the issues discussed above. The electrodes, ion optics, and housing were integrated into a monolithic block to eliminate the electrode-to-housing misalignments that can limit maximum performance. The reported integration was achieved through the use of unconventional square electrodes that enabled completely batch-fabricated devices. The device comprised solely of heavily doped silicon and silicon dioxide, thereby making the device structure thermally and mechanically robust. More importantly, the design concept can be readily extended to implement architectures such as the inclusions of prefilters, complex ion optics, and tandem quadrupoles, which can all lead to substantial improvements in performance. To begin, a brief introduction of quadrupole operation and performance metrics will be presented in Section II. The device design and optimization is covered in Section III, followed by the fabrication steps in Section IV. The experimental characterization will be summarized in Section V, and the results are discussed in Section VI.

## II. QMFs

An ideal quadrupole consists of four hyperbolic electrodes placed symmetrically in space as shown in Fig. 1(a). If  $\Phi_0$  is the applied voltage between adjacent electrodes, the established potential field can be expressed in Cartesian coordinates as

$$\Phi(x, y) = \frac{\Phi_0(x^2 - y^2)}{2r_0^2} \quad (1)$$

where  $r_0$  is the radius of the circle that is tangent to all four electrodes. If the applied signal is a combination of dc and ac

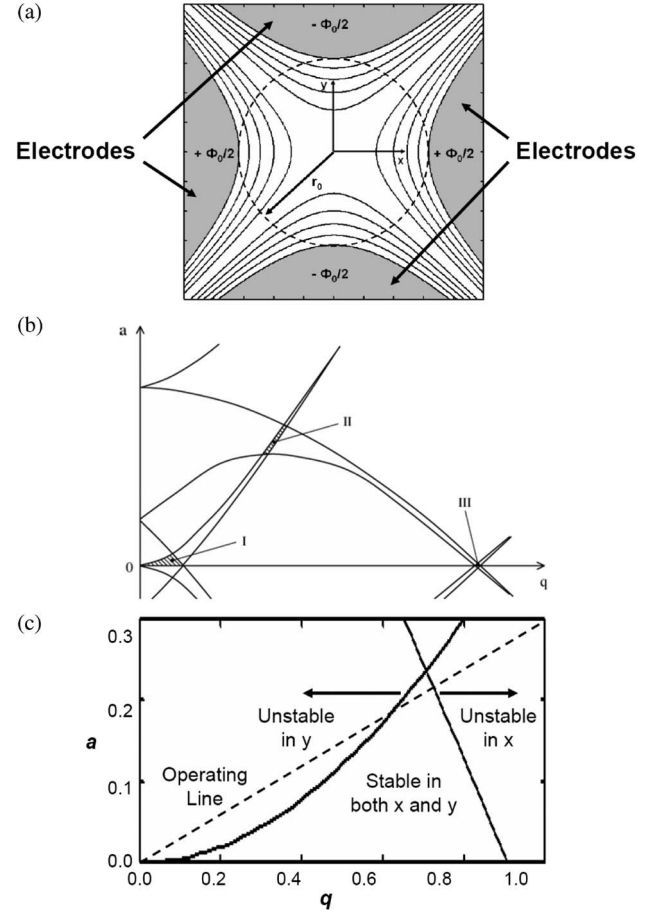


Fig. 1. (a) Cross section of ideal quadrupole with hyperbolic electrodes. (b) Mathieu stability diagram. (c) First stability region with operating line.

voltages,  $|\Phi_0/2| = U - V \cos(\omega t)$ , the equations of motion for an ion in the potential field is

$$\frac{d^2(x, y)}{dt^2} \pm \left( \frac{2e}{mr_0^2} \right) [U - V \cos(\omega t)] (x, y) = 0 \quad (2)$$

where  $e$  and  $m$  are the charge and the mass of the ion,  $U$  is the amplitude of the dc drive component, and  $V$  and  $\omega$  are the amplitude and frequency of the ac component, respectively. For most quadrupole applications,  $\omega$  is typically in the range of radio frequencies (RFs), therefore, the ac signal will be referred to as RF from now on. By making the substitutions  $u_x = x/r_0$ ,  $u_y = y/r_0$ ,  $a = 8eU/(m\omega^2 r_0^2)$ ,  $q = 4eV/(m\omega^2 r_0^2)$ , and  $\zeta = \omega t/2$ , we obtain the following Mathieu-like equation:

$$\frac{d^2 u_{x,y}}{d\zeta^2} \pm [a - 2q \cos(2\zeta)] u_{x,y} = 0 \quad (3)$$

where  $a$  and  $q$  are known as the Mathieu parameters. Depending on the values of  $a$  and  $q$ , these equations have stable and unstable solutions that can be mapped, forming the Mathieu stability diagram shown in Fig. 1(b). The boundaries stemming from positive  $a$  values on the ordinate correspond to ion motion in the  $x$ -direction, while the ones stemming from negative  $a$  values correspond to motion in the  $y$ -direction. Stability regions [shaded areas of Fig. 1(b)] are sets of operating points  $(a, q)$  where these boundaries overlap and correspond to ion motion

that is stable in both  $x$  and  $y$ . If a quadrupole is operated at an  $(a, q)$  near the corner of a stability region [Fig. 1(c)], an ion with a specific  $m/e$  will have a small range of  $U$  and  $V$  that will produce stable  $x$  and  $y$  trajectories within the device. By choosing the appropriate drive voltages, we can select the  $m/e$  that passes through the quadrupole, thus, mass filtering is achieved. A mass spectrum can be generated if the dc and RF voltages are scanned at a fixed ratio  $a/q = 2U/V$  and the number of transmitted ions are recorded as a function of  $m/e$ . A more thorough and detailed explanation of QMF operation and the associated ion dynamics is given in the literature [47], [48].

The performance of a QMF can be characterized by two key metrics, namely: 1) the mass range and 2) the resolution. The mass range is the maximum mass resolvable with a quadrupole of radius  $r_0$  given a set of operating conditions. The operating point  $(a, q)$ , the drive frequency, and the maximum applied voltage will affect this metric, but it is ultimately constrained by the electrical breakdown of the QMF and the voltages that can be supplied by the drive electronics. The resolution is the more important metric and is an indicator of how selective the mass filter is in distinguishing ions with  $m/e$  that are close in value. Resolution is generally expressed as the ratio  $R = m/\Delta m$ , where  $m$  is the mass corresponding to the peak detected and  $\Delta m$  is the peak full width at half the maximum signal intensity, often referred to as full-width half-max (FWHM). The closer the quadrupole is operated to the corner of the stability region, the smaller the peak width and the higher the resolution will be. In an actual device with electrode misalignments and finite length, the maximum resolution is limited by the accuracy of the established quadrupole field and  $n$ , the number of RF cycles that an ion spends in the QMF [48], [56]. Since the mass filtering mechanism is related to the ion trajectories, which are oscillatory in nature, we would expect the resolution to have some dependence on  $n$ . An approximation for  $n$  is  $fL/v_z$ , where  $f$  is the drive frequency,  $L$  is the quadrupole length, and  $v_z$  is the axial ion velocity. It has been determined empirically that the resolution can be given by [48]

$$R = \frac{m}{\Delta m} \cong \frac{n^2}{h} \approx \frac{1}{h} \left( f \frac{L}{v_z} \right)^2 \quad (4)$$

where  $h$  is a constant that reflects how good the mass filter is coupled with the ionizer as well as the chosen operating point  $(a, q)$ . Typical values reported for  $h$  in the first stability region [I of Fig. 1(b)] are between 10 and 20, while the values are between 0.73 and 1.43 for the second stability region [II of Fig. 1(b)] [48]. A smaller  $h$  denotes better overall performance since the resolution achieved is higher for a given  $n$ .

Most work with quadrupoles has been conducted in the first stability region, but there have been reports of operation in the second stability region (sometimes referred to as zone 3 or the intermediate stability region), leading to improved peak shape and higher resolution [53], [57]–[62]. The improvement comes from the higher fundamental frequency of the ion motion when operated in the higher stability region [48]. The increased base frequency effectively increases the number of cycles that an ion experiences, making the trajectories of the unselected

ions grow unstable quicker, resulting in improved resolution. This behavior is reflected in the smaller  $h$  values reported for the second stability region. The tradeoffs with utilizing the higher stability region are the corresponding increase in voltage needed for the larger  $(a, q)$ , which limits the maximum mass range, and the associated decrease in transmission with increased resolution. Fortunately, a more sensitive detector can be used to compensate for the diminished signal strength [35], [36]. Operation at higher pressures also increases the signal abundance, therefore, scaled-down devices can directly benefit from using the higher stability region.

### III. DESIGN AND OPTIMIZATION

From the physics of QMF operation, it is clear that devices with large aspect ratios are needed for high performance. Achieving these large aspect ratios using only microfabrication techniques requires the devices to be made in-plane to the wafer. In most commercially available quadrupoles, the electrodes have a circular cross section instead of the ideal hyperbolic shape to tradeoff performance for manufacturing simplicity. Cylindrical rods were also used in other MEMS-based QMFs, but this geometry is not readily feasible with in-plane microfabrication techniques. To address this issue, we introduced a rectangular electrode geometry that is easily produced with established microfabrication processes [63]. As cylindrical electrodes are an approximation to the ideal hyperbolic case for manufacturing simplicity, the use of rectangular electrodes is an extension of the approximation for microfabrication simplicity. This concept works because QMF operation is a boundary value problem in which the electric fields established by the various electrode geometries are very similar near the central axis of the device. The region around the central axis is where transmitted ions spend a significant portion of their flight times, and hence, we expect proper mass filtering to occur.

#### A. Design

We designed our device targeting a mass range of 400 amu and a minimum FWHM peak width of 1.0 amu since this specification has utility for a wide range of applications. With an intended operational pressure of  $\sim 1$  mtorr, the maximum quadrupole length was limited to 50 mm to ensure proper operation. The device length needs to be smaller than the gas mean free path to ensure ions will travel within the filter without collisions. A length of 30 mm was chosen so that there could be a direct comparison to some of the other reported MEMS-based quadrupoles [49]–[52].

Using (4) and the fact that  $v_z = (2E_z/m)^{1/2}$ , where  $E_z$  is the axial ion energy, we obtain

$$\Delta m = \frac{2hE_z}{f^2 L^2} \quad (5)$$

while rewriting the equation for the Mathieu parameter  $q$  gives

$$V = \pi^2 q \frac{m}{e} f^2 r_0^2. \quad (6)$$



Equations (5) and (6) were used to guide the design of our device. Assuming  $E_z = 5$  eV,  $h = 15$ , and  $\Delta m = 1$  amu, the operating frequency was calculated to be 4 MHz with  $L = 30$  mm. At this drive frequency and at an imposed maximum operating voltage  $V_{\max} = 150$  V, we found that the device radius  $r_0$  should be less than  $570 \mu\text{m}$  to achieve the desired mass range assuming a typical operating point  $(a, q) = (0.23, 0.7)$ . Clearly, a device with a smaller  $r_0$  would require less drive voltage, but there are limitations to how small  $r_0$  should be. As  $r_0$  decreases in size, the device will become more susceptible to misalignments and fringing fields that degrade performance [2], [52], [64]. Surface roughness arising from microfabrication techniques will also be much more apparent on a smaller scale, thereby increasing the amount of undesirable field distortions. Additionally, a very small device cross section would result in decreased transmission, undesirable space-charge effects, and increased difficulty in coupling ions into the QMF [2], [48].

### B. Optimization

Due to the unconventional geometry proposed, a study was conducted to optimize the critical device dimensions. From the geometric configuration of a quadrupole, we can express the potential field established by the electrodes as

$$\begin{aligned} \Phi(r, \theta) &\approx \Phi'(r, \theta) \\ &= \sum_{j=1}^{\infty} C_j \left(\frac{r}{r_0}\right)^j \cos(j\theta) + \sum_{k=1}^{\infty} S_k \left(\frac{r}{r_0}\right)^k \sin(k\theta) \end{aligned} \quad (7)$$

$$C_j = \frac{8(j+1)}{r_0^2 \pi} \int_0^{\pi/4} \int_0^{r_0} \Phi'(r, \theta) \left(\frac{r}{r_0}\right)^j \cos(j\theta) r dr d\theta \quad (8)$$

$$S_k = \frac{8(k+1)}{r_0^2 \pi} \int_0^{\pi/4} \int_0^{r_0} \Phi'(r, \theta) \left(\frac{r}{r_0}\right)^k \sin(k\theta) r dr d\theta. \quad (9)$$

Equation (7) is a general solution to Laplace's equation in cylindrical coordinates with weighting coefficients  $C_j$  and  $S_k$  [49]. From the asymmetry of the driving potential along the lines  $y = x$  and  $y = -x$  (see Fig. 2), values for  $j$  can only be 2, 6, 10, ..., while values for  $k$  can only be 4, 8, 12, .... The  $C_2$  term is the ideal quadrupole term, and the other coefficients are higher order nonideal terms. This equation emphasizes the fact that a QMF is a boundary value problem since the higher order terms have a minimal contribution to the electric potential for  $r \ll r_0$ . Optimization was conducted by minimizing the magnitude of the higher order terms with respect to the ideal  $C_2$  term.

The device cross section is shown in Fig. 2, along with dimensions that were parameterized in the optimization. Initial simulations were conducted without the housing to determine the optimal dimensions for the electrodes assuming a square aperture region. For a particular combination of  $A$ ,  $B$ , and  $C$ , the software MAXWELL 2-D from Ansoft was used to find a solution for the potential  $\Phi'(r, \theta)$ , converging with an

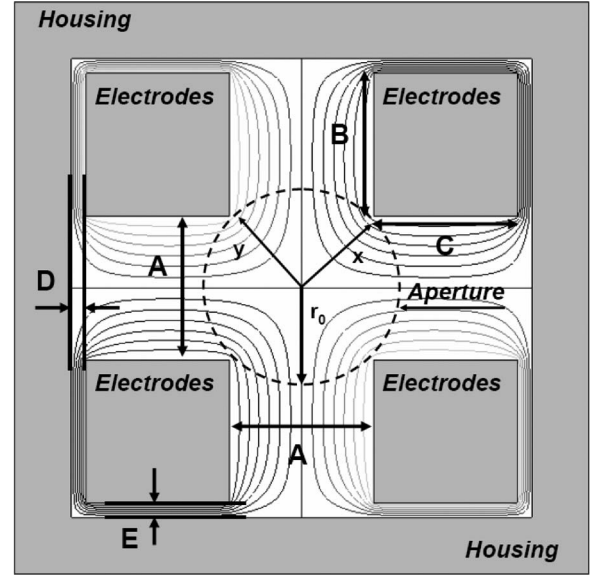


Fig. 2. Schematic cross section of the device used in simulations:  $A$  is the characteristic size of the inscribed square in the circular aperture region,  $B$  and  $C$  are the height and width of the electrodes, respectively, while  $D$  and  $E$  are the horizontal and vertical spacing between the electrodes and housing, respectively.

energy error of  $<0.001\%$ . This solution was then exported as a grid into a MATLAB script that solved for the coefficients  $C_j$  and  $S_k$  using numerical integration [49]. The results of these calculations varied depending on the grid size used so the size was kept constant for all the simulations summarized in Fig. 3(a). A grid size of  $3750 \times 3750$  was the maximum number of data points that could be processed with our analysis. The solutions varied from those of a  $3000 \times 3000$  grid by less than 1%, indicating a convergent solution. We saw that having  $B = C$  eliminated the  $S_k/C_2$  terms because of four-fold symmetry, and setting  $B \geq A$  provided a minimum in the  $C_j/C_2$  terms. Having  $B$  larger than  $A$  did not provide substantial improvements in the optimization, so  $A = B = C$  was utilized for our design.  $A = 1$  mm was selected under the impression that the effective device radius would be  $500 \mu\text{m}$ . In actuality, using  $A = 1$  mm corresponds to  $r_0 = 707 \mu\text{m}$ , which was larger than our design constraint of  $570 \mu\text{m}$ . This minor oversight essentially halved the desired mass range calculated in the design section above.

Additional simulations including the quadrupole housing were conducted with  $A = B = C = 1$  mm. Dimension  $D$  corresponds to a dimension that is set by the mask layout, thus, it was varied more substantially. On the other hand, dimension  $E$  is limited by the wafer thicknesses and the silicon etch capabilities, thus, only two values were simulated. In Fig. 3(b), we saw that setting  $D = E$  eliminated the  $S_k/C_2$  terms due to the preservation of fourfold symmetry, while the  $C_j/C_2$  term was minimized with larger values for  $D$  and  $E$ . Despite this result, dimension  $E$  was kept small due to consideration for the improved cross-wafer etch uniformity associated with shallower etch features. Additionally, dimension  $D$  was limited to  $100 \mu\text{m}$  or greater because of the maximum trench aspect ratio capable with our etch systems. Ultimately,  $D = E = 100 \mu\text{m}$  was utilized resulting in nonoptimal values for  $C_j/C_2$

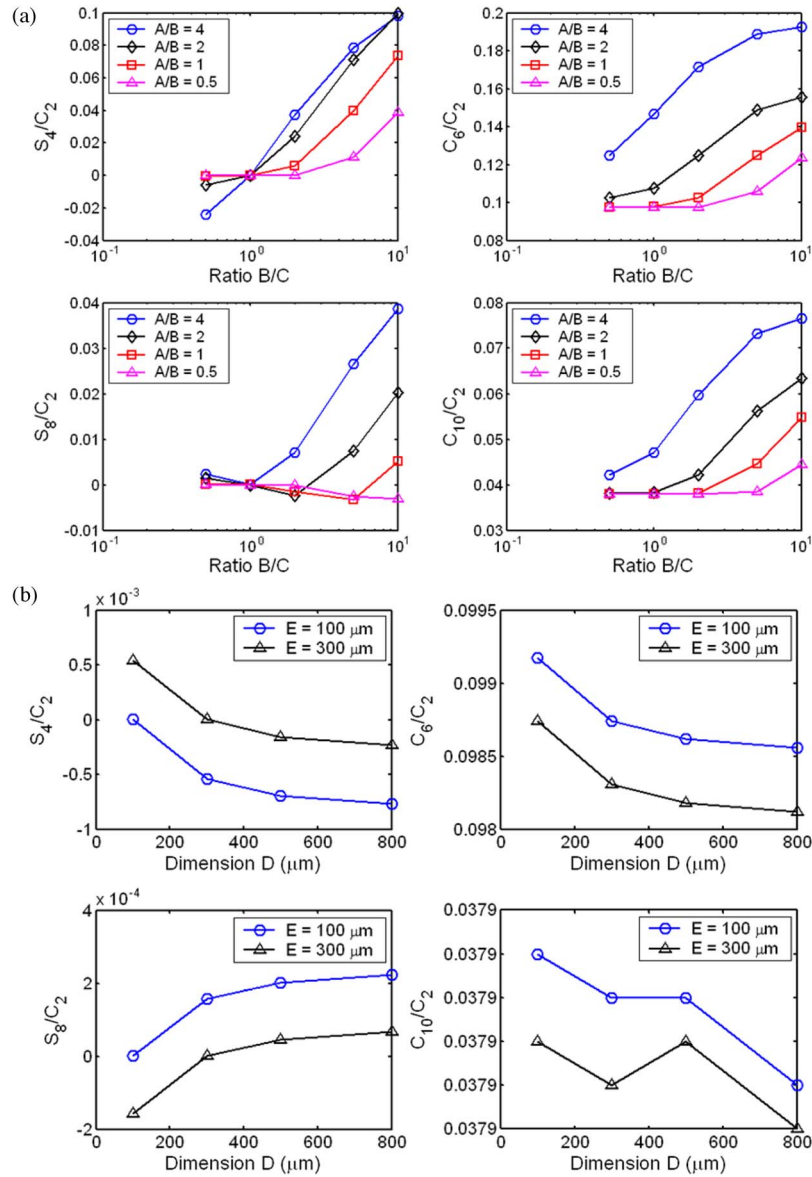


Fig. 3. (a) Coefficients for the multipole expansion with various  $A$ ,  $B$ , and  $C$ . (b) Coefficients for the multipole expansion with  $A = B = C = 1$  mm and various  $D$  and  $E$ .

TABLE I  
COEFFICIENTS OF THE POTENTIAL FIELD MULTIPOLE EXPANSION  
FOR OPTIMIZED GEOMETRIES [65]

	Circular Rods $r/r_0 = 1.128$	Square Electrodes
$C_2$	1.0016	0.7838
$C_6$	$1.2000 \times 10^{-3}$	$8.0909 \times 10^{-2}$
$C_{10}$	$-2.4325 \times 10^{-3}$	$3.2235 \times 10^{-2}$
$C_{14}$	$-2.6928 \times 10^{-4}$	$1.8101 \times 10^{-2}$

that were only  $\sim 1.5\%$  greater than the best case scenario ( $D = E = \infty$ ). The leading coefficients for our optimized square geometry are given in Table I, along with the values for an optimized cylindrical geometry [65]. It is apparent that the higher order terms are nonnegligible with respect to  $C_2$  in the square electrode case, alluding to some degree of degradation in performance [56], [66], [67]. Prior work showed that we could reduce the effects of these nonideal terms by operating in the

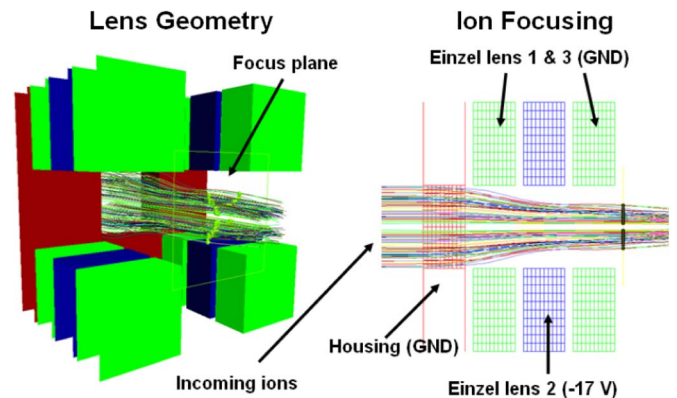


Fig. 4. Simulation of an Einzel lens with three sets of the unconventional lens elements in series.

second stability region [53], [57]–[61], thus providing a means to address the expected performance loss associated with the square electrode geometry.

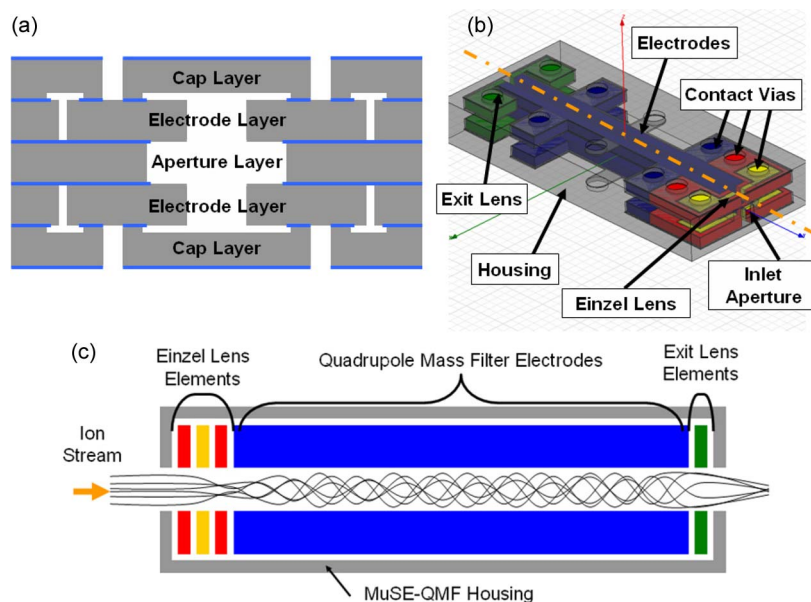


Fig. 5. (a) Cross section of the device across the width of the device. (b) Schematic of the final device. (c) Cross section along the length of the device with ion trajectories.

### C. Integrated Ion Optics

Typical ion lenses come in the shape of circular or rectangular rings, but these geometries are not compatible with our device design. To achieve the integration of ion optics, each lens component was broken into four corresponding elements. These modified lenses are identical in cross section to the QMF electrodes, thus allowing them to be formed simultaneously with the rest of the device. An Einzel lens configuration was simulated with CPO-3DS from Scientific Instrument Services to verify that the unconventional geometry was capable of focusing (Fig. 4). The results show that a stream of ions can be focused symmetrically onto a focal plane, unlike the astigmatic lenses reported for other MEMS-based quadrupoles [51], [68]. These lenses work due to the fact that the electric field sufficiently far from the lens elements are similar to those established for lenses with conventional geometries. An additional benefit of having each lens comprised of four individual elements is that it allows for beam shaping. Beam shaping can be used to improved device performance if the incoming ion beam is matched to the quadrupole acceptance [48], [61], [69], [70].

## IV. DEVICE FABRICATION

All fabrication steps were conducted in a combination of class 10 and class 100 cleanrooms at MIT's Microsystems Technology Laboratories. The reported devices comprised of five double-side polished silicon wafers that were heavily doped with antimony. The wafers had a sheet resistance of  $10\text{--}20\text{ m}\Omega/\text{cm}$ , which ensured that the silicon behaved as similar to a metal as possible. To implement the design outlined in Fig. 5, two  $500 \pm 5\text{ }\mu\text{m}$ -thick wafers were used as the capping layers, two  $1000 \pm 10\text{ }\mu\text{m}$ -thick wafers made up the electrode layers, and a third  $1000 \pm 10\text{ }\mu\text{m}$ -thick wafer was used for the aperture layer. The wafers, with a total thickness variation of  $< 2\text{ }\mu\text{m}$ , came from Ultrasil Corporation (Hayward, CA) with  $0.5\text{ }\mu\text{m}$  of thermal oxide initially grown to serve as a protective layer.

All the wafers began with the same processing steps, streamlining the fabrication. Alignment marks were placed on both sides of the wafers using contact photolithography with thin resist. The alignment marks were defined with a buffered-oxide etch to remove the exposed protective oxide and was followed by a shallow reactive ion etch (RIE) to pattern the silicon. The wafers were then piranha cleaned ( $4:1\text{ H}_2\text{SO}_4:\text{H}_2\text{O}_2$ ) to remove the photoresist and underwent a 49% hydrofluoric acid bath to strip off all the oxide. The wafers were then RCA cleaned prior to a thick  $2.5\text{ }\mu\text{m}$  wet oxidation at  $1050\text{ }^\circ\text{C}$ , followed by a  $250\text{ nm}$  low-pressure chemical vapor deposition (LPCVD) of low-stress silicon nitride. The nitride layer was used to preserve the quality of the bond interfaces throughout subsequent process steps.

### A. Cap and Aperture Wafers

The cap wafers and aperture wafer were processed in a very similar manner as depicted in Fig. 6(a) and (b). For each wafer, thick photoresist was spun on both sides followed by double-sided contact photolithography. The exposed nitride and oxide were removed using a two-step RIE on each side, and was followed by a deep RIE (DRIE) on both sides to pattern the silicon. The wafers were mounted onto a quartz handle wafer after the initial DRIE to ensure proper etching of the back side. After the second etch, the wafers were dismounted from the handle wafers with acetone, cleaned with piranha, and ashed in oxygen plasma for 1 h. The cap wafers had a shallow  $100\text{ }\mu\text{m}$  trench patterned on the front side, and a  $400\text{ }\mu\text{m}$  through-wafer etch to produce the contact vias on the back side. The aperture wafer had the same pattern etched to a depth of  $500\text{ }\mu\text{m}$  on both sides to ensure symmetry of the devices.

### B. Electrode Wafers

The processing of the electrode wafers is outlined in Fig. 6(c). The wafers began with thick resist spun on both sides followed by double-sided contact photolithography of the same

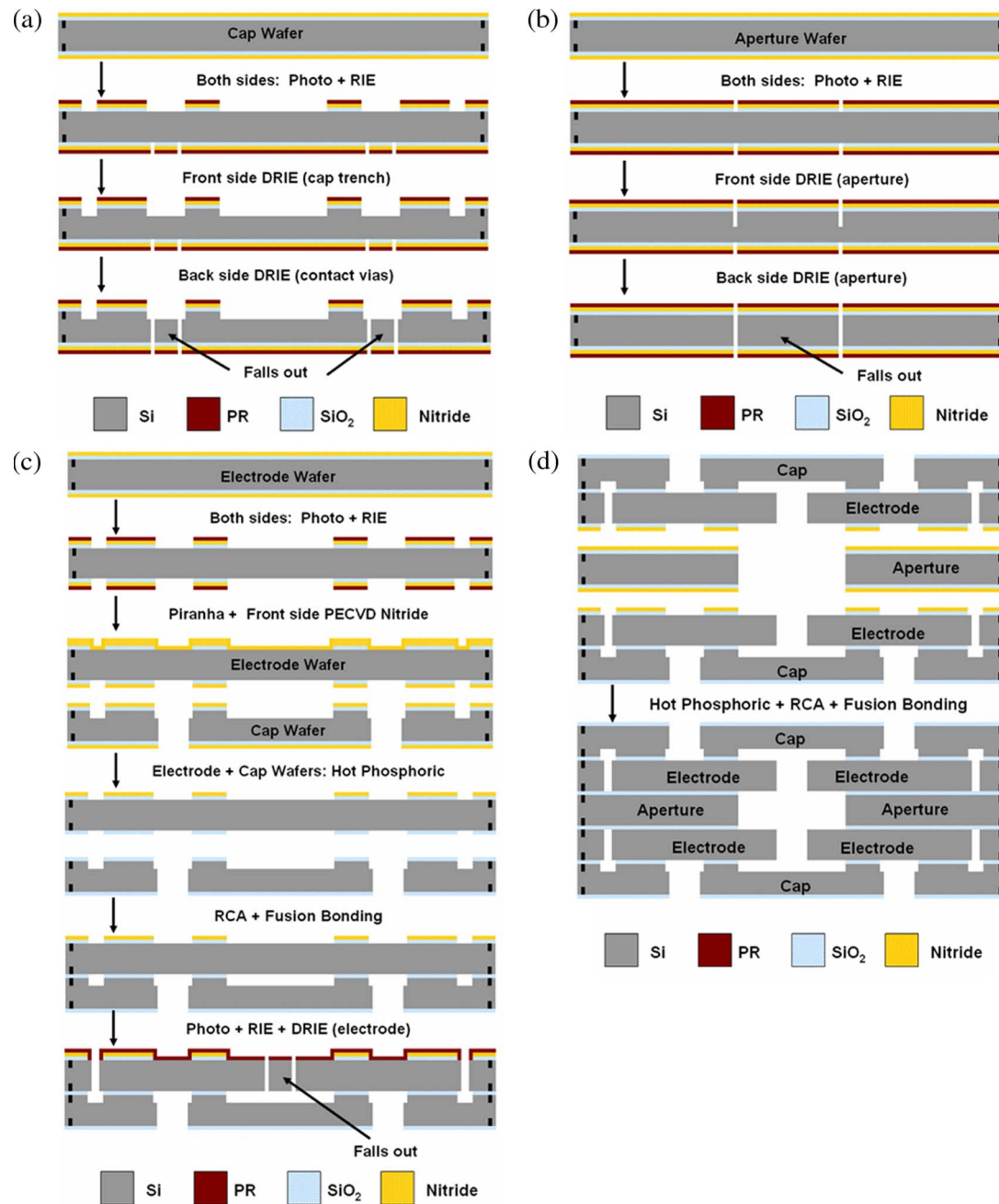


Fig. 6. Device process flows. (a) Cap wafers. (b) Aperture wafer. (c) Electrode wafers. (d) Final steps.

pattern. The exposed nitride and thick oxide were removed using a two-step RIE on each side followed by a resist strip and wafer cleaning with piranha. The wafers then had 1.4  $\mu\text{m}$  of low-stress nitride deposited on one side through plasma-enhanced chemical vapor deposition (PECVD) to serve as a timed-etch mask. The processed cap wafers and the electrode wafers were then placed into phosphoric acid at 165  $^{\circ}\text{C}$  for 1.5 h. This step removed all the LPCVD nitride on the cap wafers and left  $\sim 150$  nm of LPCVD nitride on one side of the electrode wafers. The wafers were RCA cleaned and then aligned so the side of the cap wafers with the shallow trench was contacted with the nitride-free surface of the electrode wafers. The two wafer pairs were fusion bonded with initial contact made in vacuum, compression with 2500 N for 12+ h, and a 1-h

anneal at 1000  $^{\circ}\text{C}$  in nitrogen. The cap/electrode stacks then had thick photoresist spun on the face with LPCVD nitride, and the pattern for the electrodes and lens elements was transferred. The exposed pattern was etched by a two-step RIE to remove the nitride and thermal oxide before being mounted onto a quartz handle wafer. The mounted stacks were then etched with a 1000  $\mu\text{m}$  DRIE to define the electrodes and lens elements. Finally, the stacks were dismounted in acetone, cleaned with piranha, and ashed in oxygen plasma for 1 h.

### C. Final Steps

The final process steps are shown in Fig. 6(d). The two cap/electrode stacks and the aperture wafer were all placed into



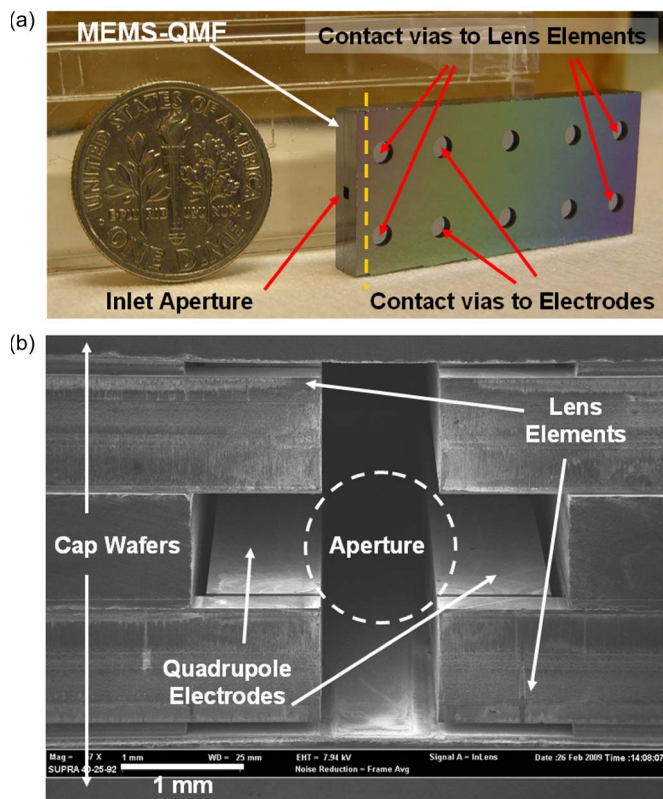


Fig. 7. (a) Completed device. (b) Scanning electron micrograph of the cross section along the dashed line in (a).

phosphoric acid at 165 °C for 1.5 h to ensure that all the remaining LPCVD nitride was removed from the bonding surfaces. The stacks and aperture wafer were RCA cleaned, aligned with the aperture wafer sandwiched between the two stacks, and then fusion bonded. The bonded five-wafer stack was die sawed to complete the devices by simultaneously opening the inlet and outlet while separating the individual dies (Fig. 7). The accuracy of each photo alignment step was measured with an EVG TBM8 and quantified to be within  $\pm 2.5 \mu\text{m}$ , while the bonding alignment has a similar accuracy. Since the device processing required five front-to-backside photo alignments and four bond alignments, we estimated a maximum total misalignment of  $\pm 7.5 \mu\text{m}$  using error propagation. Additionally, a study using simulations showed that electrode misalignments on the order of  $\pm 10 \mu\text{m}$  resulting from our fabrication methodology will have a minor impact on the expected performance [65].

The completed wafer stack produced 11 out of 14 devices that could be utilized since three were damaged during die sawing. For the remaining devices, we encountered shorting issues between the electrodes, ion optics, and the housing. We determined that this problem originated from stringers (residual slivers of silicon) that formed during etching of the electrode wafers, as well as from particles generated during the die saw step. An ultrasonic clean with solvents was used to alleviate some of the shorting issues, but it was only moderately successful. The cleaning process damaged a majority of the devices due to weakened electrodes from stress concentration resulting from a poor mask design. Stringer formation, particle generation, and stress concentration are all problems that will

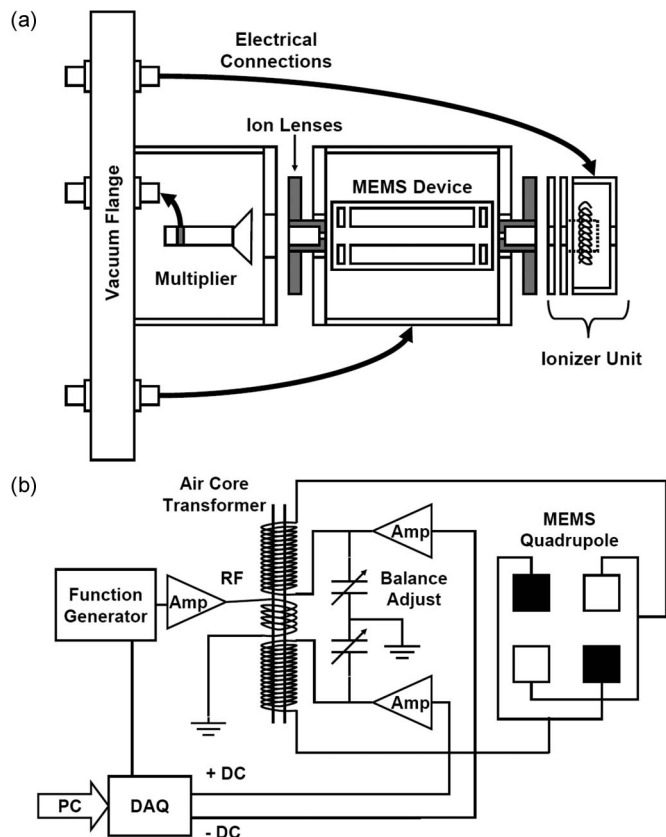


Fig. 8. (a) Schematic of vacuum flange mount. (b) Drive circuit schematic.

be resolved in the next generation of devices. Ultimately, we found three undamaged dies with functional quadrupole electrodes, but shorting issues persisted with some of the ion optic elements. Only one device with the least amount of shorting was utilized in the characterization experiments.

## V. EXPERIMENTAL EVALUATION

Characterization of the MEMS quadrupole was carried out in an in-house testing facility. Several experiments were conducted to determine the capabilities of our square electrode QMF. The first test evaluated the functionality of the integrated ion lens which would be utilized throughout the testing. Subsequent experiments were used to benchmark the performance of our device. We wanted to identify the maximum mass range achievable, the minimum peak width attainable, and the ultimate resolution that could be demonstrated with this new class of chip-scale quadrupole.

### A. Experimental Setup

The device was held in a custom-made jig that made electrical contact to the electrode elements. Pogo pins affixed to the jig extended through the contact vias to reach the electrodes. The jig and device were then mounted into an aluminum housing that was part of the vacuum flange mount depicted in Fig. 8(a). The flange mount also consists of a Channeltron electron multiplier that serves as the detector, a Slim-Line electron impact ionizer from Ardara Technologies (Ardara, PA), stainless-steel



ion lenses, and associated electrical wiring for the various components. The ionizer and lenses were controlled with a filament power supply and an optics power supply from Ardara Technologies (Ardara, PA), while the Channeltron was powered by a Keithley 248 high-voltage power supply. The assembled flange mount was then placed onto a vacuum system with a turbo pump that can reach a base pressure of  $1 \times 10^{-8}$  torr. While the system pumped down, the flange was connected to the drive circuit and all other necessary electrical connections were made. A valve system introduced air, argon, or perfluorotributylamine (a standard calibration compound also known as FC-43) into the chamber to be analyzed. Before any mass spectra were taken, the selected analyte was stabilized to a pressure of  $\sim 3 \times 10^{-5}$  torr. This pressure was chosen due to the recommended operating pressure of the commercial ionizer and detector. During testing, the signal from the detector was amplified through a Stanford Research Systems SR570 low-noise current preamplifier and collected through an NI USB-6259 data acquisition (DAQ) card to produce the mass spectrum.

The quadrupole segment of our device was driven with the drive circuit schematic shown in Fig. 8(b). The RF component of the drive signal originated from a function generator that set the frequency and initial maximum amplitude. During mass scanning, the voltage amplitude was modulated by a control voltage outputted by the DAQ card. The modulated signal then passed a wideband amplifier (Amplifier Research 150A100B) that increased the amplitude of the original signal before entering a hand-made air-core transformer. The transformer split the signal into two components that were  $180^\circ$  out of phase while stepping up the voltage once more. Variable capacitors were included in the circuit to balance the RF amplitudes, compensating for variations arising from the transformer and other passive components. The dc drive components stemmed from analog outputs on the DAQ card, which have a range of  $\pm 10$  V. This output was then amplified by operational amplifiers (Apex PA420CX) set in a noninverting amplifier configuration with high-precision resistors. The amplified dc signals were then combined with the RF components at the center tap of the transformer, producing the appropriate quadrupole drive signals. The DAQ card was interfaced to a personal computer with software written in LabVIEW that set the operation conditions, scanned the RF and dc amplitudes, acquired the detector signal, and generated the spectrum. The DAQ card has a maximum sampling rate of 1.25 MS/s, permitting a scan from 0 to 650 amu with ten data points per amu and 100 averages per point in about 2 s.

### B. Testing Procedure

Experimentation was conducted in the following manner. The operating frequency was selected, and the appropriately sized air-core transformer was attached to the quadrupole drive circuit. Capacitors were added in parallel to the transformer to fine tune the resonance frequency. The RF voltage corresponding to the desired mass range was calculated, and the gain on the wideband amplifier was adjusted to match this voltage. Next, the analyte was introduced into the vacuum

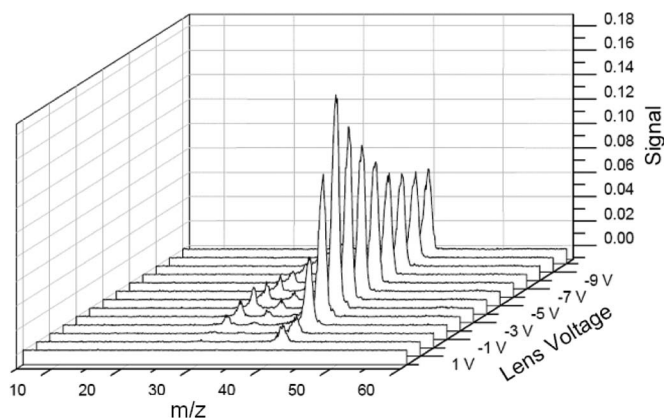


Fig. 9. Mass spectra for argon with trace leakage of air at 3.5 MHz in the first stability region and ion energy of 3.0 eV for various integrated inlet lens voltages.

chamber, and the ionizer and detector were turned on. The quadrupole was initially operated in RF only mode, allowing ions of all  $m/e$  values to pass, and the lens voltages were adjusted until the transmitted signal was maximized. After this optimization, the quadrupole was switched to mass filtering mode, and minor adjustments were made to the drive signals and electronics to improve the detected mass spectrum. At this point, the axial ion energy was adjusted to find a good balance between transmission and peak shape. The ion energy is defined as the potential difference between the ion region (ionizer volume where the ions are created) and the pole bias (centerline potential between the quadrupole electrodes), which is typically at ground. Spectra were generated using a linear scan line (fixed  $a/q$  ratio) resulting in mass peaks with constant resolution [47].

### C. Validation of Ion Optics

To evaluate the functionality of the integrated ion optics, the lenses were initially grounded so that the voltages on the external optics (stainless-steel lenses), and the ionizer could be optimized first. Once a good mass spectrum was obtained, the integrated inlet lens elements had their voltages varied to determine how the optics affected the spectrum. In Fig. 9, we can clearly see enhanced transmission when the inlet lens voltage was set to  $-3$  V. The same effect was demonstrated during operation in the second stability region, validating that the atypical lens geometry can be used to improve device performance. Clearly, good control of the device entrance conditions leads to better performance [61]. The integrated exit lens was kept at ground due to shorting issues but a functional exit lens would lead to further increases in transmission.

### D. Maximum Mass Range

FC-43 was used as the calibration compound for this experiment due to the abundant high-mass peaks associated with its spectrum. The device was driven at 1.8 MHz, the lowest resonant frequency possible with our test system, to maximize the mass that could be detected. We obtained a spectrum that demonstrated a mass range of 650 amu while showing

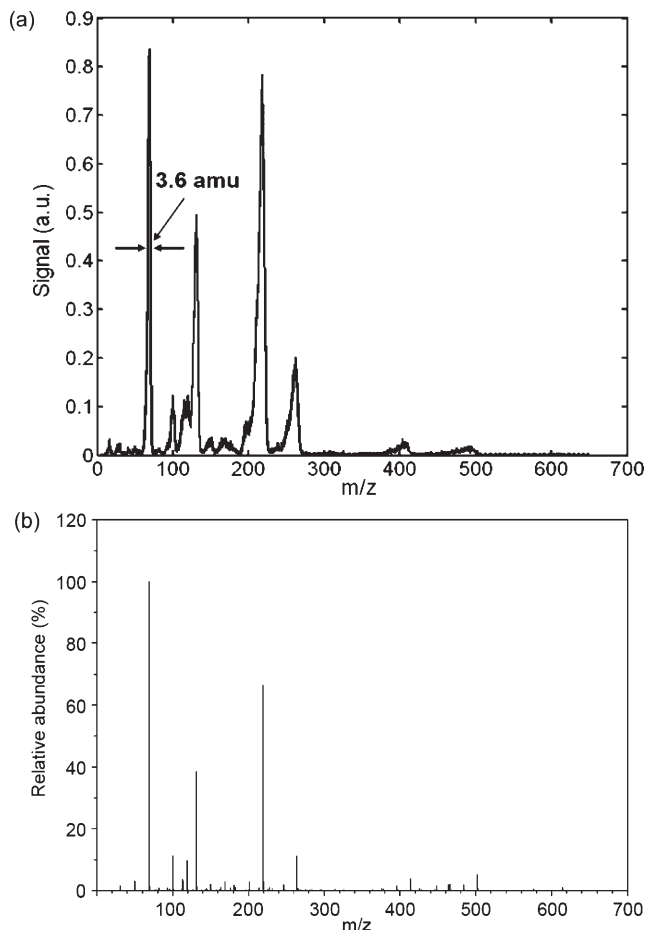


Fig. 10. (a) Mass spectrum for FC-43 at 1.8 MHz in the first stability region and ion energy of 3.5 eV. (b) NIST library spectrum for FC-43.

good correlation with the National Institute of Standards and Technology (NIST) library spectrum for FC-43 (Fig. 10). It is also important to mention the asymmetrical peak shapes apparent in this spectrum. The low-mass tails of the peaks rises substantially slower than the high-mass tails falls, giving an indication of precursor peak formation [66], [67]. Looking at the main peaks of our analyte, peak widths of 3.6 and 6.5 amu were achieved at masses 69 and 131, respectively, corresponding to a resolution of  $\sim 20$ . For the same spectrum, peak widths of 7.8 and 9.8 amu were obtained at masses 219 and 264, respectively, indicating an improved resolution of  $\sim 28$ . The change in resolution at the higher masses was most likely due to the nonlinearity of the RF amplifier. An increase in the  $a/q$  ratio during scanning would produce a mass peak with a higher resolution, while a decrease would result in lower resolution. Since higher resolution results in decreased signal intensity, this nonlinearity also explains why the peak for mass 614 is not apparent in Fig. 10(a).

#### E. Minimum Peak Width

From (5), we know that a higher driving frequency will produce a smaller peak width, but the mass range will be limited as a result. Due to the reduced detectable mass, the analyte was switched to argon in order to obtain useful spectra.

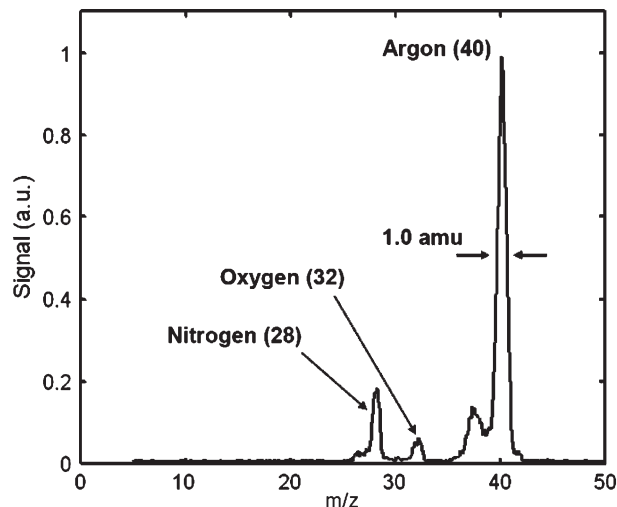


Fig. 11. Mass spectrum for argon with trace leakage of air at 4.0 MHz in the first stability region and ion energy of 3.0 eV.

For this experiment, the device was driven at 4.0 MHz, the highest frequency that could be utilized with our hand-wound transformers. In Fig. 11, we can see the peak for argon at mass 40 as well as peaks for nitrogen and oxygen at masses 28 and 32, respectively. The appearance of nitrogen and oxygen was due to a trace leakage of air into our argon line. From this spectrum, we demonstrated a peak width of 1.0 amu at mass 40 and a peak width of 0.7 amu at mass 28, both corresponding to a fixed resolution of  $\sim 40$ . We can also clearly see the existence of precursor peaks on the low-mass side of the detected peaks. These undesirable artifacts are a direct result of the higher order nonideal terms associated with the square electrode geometry [66], [67]. Despite their appearance, we can still clearly identify the distinct species within the analyte.

To evaluate the performance improvement associated with using a higher stability zone, the device was driven at 2.0 MHz in the second stability region. The drive frequency was reduced because of the larger voltages required to detect a given mass [ $q$  increases by a factor of four in (6)]. In Fig. 12, we show a peak width of 0.5 amu at mass 40 corresponding to a resolution of  $\sim 80$ , while a peak width of 0.3 amu at mass 28 demonstrates a resolution of  $\sim 93$ . Compared to Fig. 11, we have doubled the resolution utilizing the second stability region despite operating at half the frequency. We can also see that the precursor peaks were substantially reduced or eliminated, drastically improving the peak shape. This result demonstrates that operation in the second stability region is a viable method for addressing the performance degradation associated with using the square electrode geometry.

#### F. Transmission Versus Resolution

To probe the ultimate resolution of our device, we generated plots of transmission versus resolution (RT curves). These curves display how transmission falls as resolution increases and can be used to give an estimate of the maximum resolution achievable. The argon with residual air was again used as the analyte, and all experiments were conducted in the first stability region. Once a good spectrum was obtained, the transmission

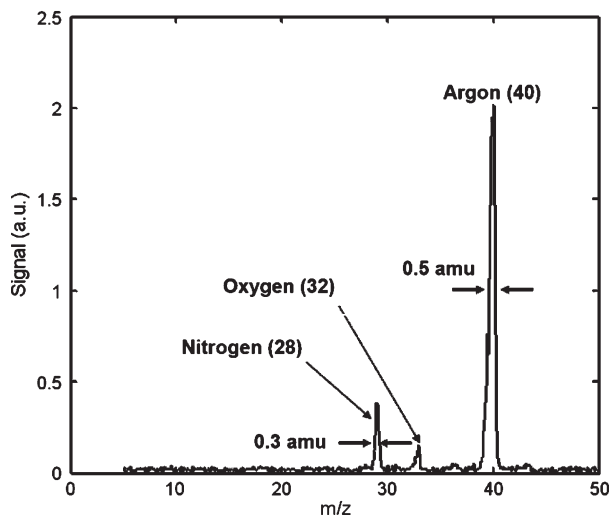


Fig. 12. Mass spectrum for argon with trace leakage of air at 2.0 MHz in the second stability region and ion energy of 5.0 eV.

was recorded as the resolution was varied by changing the Mathieu parameter  $a$  in the test software. No other adjustments were made to the testing system or the software. An increased  $a$  produced lower transmission and higher resolution, while the reverse was true for a decreased value. A fit line was made to the data points, and the ultimate resolution was defined to be the resolution at 1% relative transmission.

Fig. 13 shows various RT curves for our device at different operating frequencies along with their corresponding ion energies. From our data, we estimated an ultimate resolution of  $\sim 21$  at 2.0 MHz,  $\sim 30$  at 3.0 MHz,  $\sim 36$  at 3.5 MHz, and  $\sim 42$  at 4.0 MHz. These results appear to show resolution having a near-linear dependence on frequency, which deviates from the square dependence prescribed in (4). This deviation can be partially explained by the phenomenon described by Dawson [48] and Titov [71]. They state that there will be a maximum number of RF cycles that an ion can spend within a quadrupole before the constructional misalignments begin to add up resulting in a deviation from the expected resolution performance. By extension, it is very likely that the higher order field components of our square geometry introduce a consistently large amount of nonidealities in our quadrupole field that prevents the device from achieving the conventional frequency dependence.

## VI. DISCUSSION

Our experimental results show performance metrics that are quite comparable to most other reported MEMS-based quadrupoles (see Table II). With operation in the first stability region, we demonstrated a maximum mass range of 650 amu, a minimum peak width of 1.0 amu, and a resolution of  $\sim 40$ . These specifications are in good agreement with our targeted mass range of 400 amu and peak width of 1.0 amu, but they were not achieved simultaneously. Equations (5) and (6) give a good estimate for the expected performance, but there are many factors that are not accounted for. The actual operation of a quadrupole is quite complex and is usually only understood through simulations with numerous ion trajectories [72], [73].

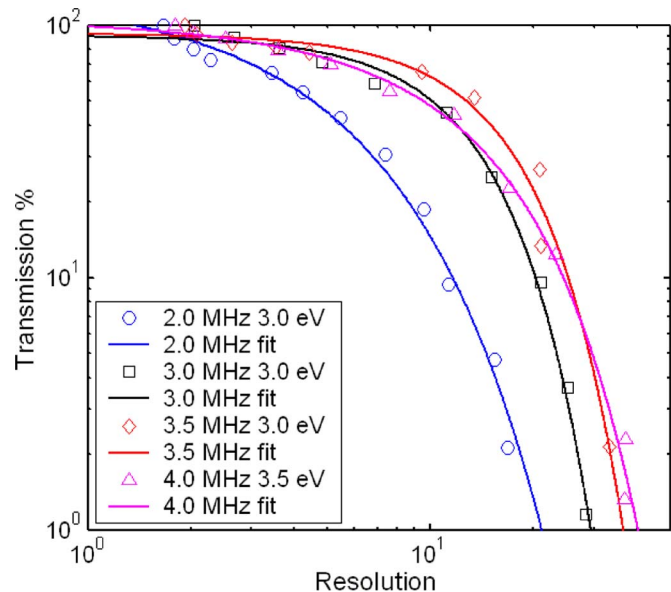


Fig. 13. Transmission versus resolution curves using argon.

Ion coupling issues, fringing fields, misalignments, geometric considerations, device design, and drive electronics all contribute to the differences between theoretical and experimental performance.

One of the main limiting factors to demonstrating high performance was the large capacitance associated with our device design and testing setup. By measuring the coil inductance and experimentally determining the circuit resonance frequency, a total load capacitance of 370 pF was calculated. We estimated that 300 pF of this load comes from parasitics in the device contact pads, 50 pF from the coaxial cabling used, and the remaining 20 pF from the quadrupole electrodes. Simulations using MAXWELL 2-D showed that our reported design results in a device capacitance of  $\sim 4.55$  pF/cm, whereas the ideal case with no housing gives  $\sim 0.88$  pF/cm. The fivefold increase in capacitance arising from the proximity of the quadrupole electrodes to the housing is a concern but the additional parasitics arising from the current design only amounts to  $\sim 11$  pF. Parasitics coming from the contact pads clearly dominates the device capacitance, affecting the capabilities of the drive electronics used for our experiments. The resonance frequency of the LC tank (inductor-capacitor resonant circuit) formed by our device and the air-core transformer was lower than desired, and the impedance was also quite small. Due to the lowered operating frequency, our resolution was degraded, but we were also unable to operate at higher frequencies that were off resonance. The low impedance of the circuit made it difficult to sustain large voltages off resonance without sufficient power. Drawing high power from the RF amplifier resulted in nonlinear behavior of the RF signal that led to poor control of the operating point. A smaller device capacitance, reduced parasitics, and a custom circuit that includes feedback for the drive signals will substantially improve the performance that can be achieved with our quadrupole.

Other issues affecting the performance of our device stem from the use of electrodes with a square cross section. During testing at low frequencies (1.5–2.0 MHz), we found that the



TABLE II  
DATA SUMMARY FOR PERFORMANCE METRICS OF FULL SPECTRA REPORTED IN THE LITERATURE AT FWHM

Group	Mass Range	Resolution @ $m/e$	$r_0$ ( $\mu\text{m}$ )	$L$ (mm)	$f$ (MHz)	$E_z$ (eV)
Liverpool [40]	50	32 <sup>^</sup> @ 40	217	30	6	13.5
MIT [43]	650	36 @ 69	690	90	1.44	13.6
	50	70* @ 28	690	90	2.0	60
	250	18 @ 69	435	37	4	40
Microsaic [42]	400	200 @ 219	217	30	6	5
MIT	650	19 @ 69	707	30	1.8	3.5
	50	40 @ 40	707	30	4.0	3.0
	50	90* @ 28	707	30	2.0	5.0

<sup>^</sup> denotes value extracted from analysis of reported spectra

\* denotes resolution obtained with operation in the second stability region

RF and dc amplitudes needed to be increased by a factor of  $\sim 1.27$  from the calculated voltages to properly calibrate the device. This compensation factor led to the realization that the effective magnitude of the  $C_2$  term listed in Table I needs to be increased to unity for proper mass detection. From this result, we know that the mass range for our device will be decreased by 27% compared to a conventional quadrupole with the same device radius if the drive voltages remain unchanged. At higher frequencies (3.0–4.0 MHz), the compensation factor needed for the RF approached  $\sim 1.0$ , while the dc compensation remained at  $\sim 1.27$ . After careful investigation, parasitic inductance in the testing jig was believed to be the cause of this strange behavior. An improved testing jig can be used to alleviate this issue in future experiments.

We also experimentally determined that the high-resolution corner of the first stability region was located at an operating point of  $(a, q) = (0.28, 0.7)$  instead of the conventional  $(a, q) = (0.23, 0.7)$ . This observation indicates that there could be a new stability diagram associated with our device. The Mathieu stability diagram shown in Fig. 1(b) is the graph of stable solutions for an ideal quadrupole that is infinitely long. We would expect some differences due to our square electrode device geometry and the finite length. The new value for  $a$  implies that the dc drive signal needed to achieve high resolution is  $\sim 22\%$  larger than that for a conventional quadrupole. This increase is in addition to the compensation factor described above. Another possible reason for the change in location of the high-resolution corner is voltage drops within the testing circuit and testing jig. This possibility requires further investigation and can be addressed by using a feedback circuit. A modified stability diagram and the near-linear trend depicted in the RT curves of Fig. 12 would allude to some new ion dynamics. These results motivate further studies on ion behavior for quadrupoles with unconventional electrode geometries.

Despite the complications and issues encountered with testing our devices, we were able to demonstrate several new and advantageous features. Looking at the ion energies in Table II, we can see that our device was able to obtain spectra with the lowest ion energy. This result was most likely due to our integrated housing, which shields ions from the fringing fields at the inlet, thereby improving entrance conditions. We also showed that using the second stability region is the ideal operating mode for our devices. If we compare the spectra shown in Figs. 11 and 12, we clearly see that the second stability region is able to demonstrate improved resolution and peak shape without affecting the relative abundance. Furthermore, the RF

drive voltages needed to obtain both spectra are essentially the same. The larger operating  $(a, q)$  associated with the second stability region (approximately a fourfold increase in  $q$ ) is compensated by driving the device at half the frequency. In general, the second stability region is advantageous for MEMS-based quadrupoles. The decreased drive voltages associated with the smaller dimensions make using the second stability region a viable option, while the higher resolution achieved can address the increased relative misalignments inherent in scaled-down devices.

Finally, we showed the successful operation of integrated ion optics with an unconventional geometry (Figs. 4 and 9). This concept can easily be extended to more complex features such as Einzel lenses as well as prefilters and postfilters to improve performance [74], [75]. A simple change in the mask layout can be used to produce these additional features. A more interesting architecture that can be implemented is the tandem quadrupole. Du and Douglas reported tandem quadrupoles that were able to improve resolution by at least a factor of ten over an equivalent quadrupole of the same combined length [76]. Our technology is suited to this architecture due to the alignment precision needed between the two quadrupoles for proper operation. Additionally, we can think of using our technology to enable tandem mass analyzers (TOF/QMF, RIT/QMF, triple quads, etc.) or even more complex systems. Other MEMS-based quadrupole technologies cannot readily accomplish this level of integration due to the increased difficulty associated with assembling a multitude of electrodes.

## VII. CONCLUSION

Completely batch-fabricated chip-scale QMFs with the electrodes, ion optics, and housing integrated into a monolithic block have been fabricated and characterized. These devices show promising performance comparable with other MEMS-based quadrupoles despite the square electrode geometry. A mass range of 650 amu at 1.8 MHz was demonstrated in the first stability region, and a minimum peak width of 0.3 amu at 2.0 MHz was achieved in the second stability region. The experimental data showed a maximum resolution of  $\sim 90$  and validated the functionality of integrated optics with unconventional lens geometry. More importantly, the process flow and design concept utilized for our devices can be extended to smaller quadrupoles and complex architectures, paving the way for a new class of miniaturized mass spectrometers. Operation in the second stability region led to improved peak shape

and higher resolution, thereby providing a means to enhance the mass spectra attainable from less than ideal quadrupoles. Overall, this paper has presented devices with several distinct advantages over other MEMS-based QMF technologies, and has shown data that allude to new ion dynamics which should be explored.

#### ACKNOWLEDGMENT

The authors would like to thank the staff at MIT's Microsystems Technology Laboratories for their help throughout the fabrication of the devices and Dr. R. Pedder (Ardara Technologies, Ardara, PA) for the guidance in the experimental assembly and characterization of the quadrupoles.

#### REFERENCES

- [1] E. R. Badman and R. G. Cooks, "Special feature: Perspective, miniature mass analyzers," *J. Mass Spectrom.*, vol. 35, no. 6, pp. 659–671, Jun. 2000.
- [2] S. Boumsellek and R. J. Ferran, "Trade-offs in miniature quadrupole designs," *J. Amer. Soc. Mass Spectrom.*, vol. 12, no. 6, pp. 633–640, Jun. 2001.
- [3] Z. Ouyang, R. J. Noll, and R. G. Cooks, "Handheld miniature ion trap mass spectrometers," *Anal. Chem.*, vol. 81, no. 7, pp. 2421–2425, Apr. 2009.
- [4] Z. Ouyang and R. G. Cooks, "Miniature mass spectrometers," *Annu. Rev. Anal. Chem.*, vol. 2, pp. 187–214, 2009.
- [5] O. J. Orient and A. Chutjian, "A compact, high-resolution Paul ion trap mass spectrometer with electron-impact ionization," *Rev. Sci. Instrum.*, vol. 73, no. 5, pp. 2157–2160, May 2002.
- [6] P. M. Holland, A. Chutjian, M. R. Darrach, and O. J. Orient, "Miniaturized GC/MS instrumentation for *in situ* measurements: Micro gas chromatography coupled with miniature quadrupole array and Paul ion trap mass spectrometers," *Proc. SPIE*, vol. 4878, pp. 1–7, 2003.
- [7] J. M. Wells, E. R. Badman, and R. G. Cooks, "A quadrupole ion trap with cylindrical geometry operated in the mass-selective instability mode," *Anal. Chem.*, vol. 70, no. 3, pp. 438–444, Feb. 1998.
- [8] O. Kornienko, P. T. A. Reilly, W. B. Whitten, and J. M. Ramsey, "Micro ion trap mass spectrometry," *Rapid Commun. Mass Spectrom.*, vol. 13, no. 1, pp. 50–53, Jan. 1999.
- [9] O. Kornienko, P. T. A. Reilly, W. B. Whitten, and J. M. Ramsey, "Electron impact ionization in a microion trap mass spectrometer," *Rev. Sci. Instrum.*, vol. 70, no. 10, pp. 3907–3909, Oct. 1999.
- [10] E. R. Badman and R. G. Cooks, "A parallel miniature cylindrical ion trap array," *Anal. Chem.*, vol. 72, no. 14, pp. 3291–3297, Jul. 2000.
- [11] G. E. Patterson, A. J. Guymon, L. S. Riter, M. Everly, G. Griep-Raming, B. C. Laughlin, Z. Ouyang, and R. G. Cooks, "Miniature cylindrical ion trap mass spectrometer," *Anal. Chem.*, vol. 74, no. 24, pp. 6145–6153, Dec. 2002.
- [12] D. Smith and P. R. Cromey, "An inexpensive, bakeable quadrupole mass spectrometer," *J. Phys. E, Sci. Instrum.*, ser. 2, vol. 1, no. 5, pp. 523–527, May 1968.
- [13] R. J. Ferran and S. Boumsellek, "High-pressure effects in miniature arrays of quadrupole analyzers for residual gas analysis from  $10^{-9}$  to  $10^{-2}$  Torr," *J. Vac. Sci. Technol. A, Vac. Surf. Films*, vol. 14, no. 3, pp. 1258–1265, May 1996.
- [14] S. Boumsellek and R. J. Ferran, "Miniature quadrupole arrays for residual and process gas analysis," *J. IEST*, vol. 42, pp. 27–31, Jan. 1999.
- [15] D. H. Holkeboer, T. L. Karandy, F. C. Currier, L. C. Frees, and R. E. Ellefson, "Miniature quadrupole residual gas analyzer for process monitoring at millitorr pressures," *J. Vac. Sci. Technol. A, Vac. Surf. Films*, vol. 16, no. 3, pp. 1157–1162, May 1998.
- [16] J. Wang, X. Zhang, F. Mao, M. Xiao, Y. Cui, D. den Engelsens, and W. Lei, "Study of a micro chamber quadrupole mass spectrometer," *J. Vac. Sci. Technol. A, Vac. Surf. Films*, vol. 26, no. 2, pp. 239–243, Mar. 2008.
- [17] T. J. Cornish and R. J. Cotter, "High-order kinetic energy focusing in an end cap reflectron time-of-flight mass spectrometer," *Anal. Chem.*, vol. 69, no. 22, pp. 4615–4618, Nov. 1997.
- [18] R. J. Cotter, C. Fancher, and T. J. Cornish, "Miniaturized time-of-flight mass spectrometer for peptide and oligonucleotide analysis," *J. Mass Spectrom.*, vol. 34, no. 12, pp. 1368–1372, Dec. 1999.
- [19] T. T. King, S. A. Getty, P. A. Roman, F. A. Herrero, H. H. Jones, D. M. Kahle, B. Lynch, G. Suarez, W. B. Brinkerhoff, and P. R. Mahaffy, "Simulation of a miniature, low-power time-of-flight mass spectrometer for *in situ* analysis of planetary atmospheres," *Proc. SPIE*, vol. 6959, no. 69590E, pp. 1–15, 2008.
- [20] M. P. Sinha and A. D. Tomassian, "Development of a miniaturized, light-weight magnetic sector for a field-portable mass spectrograph," *Rev. Sci. Instrum.*, vol. 62, no. 11, pp. 2618–2620, Nov. 1991.
- [21] J. A. Diaz, C. F. Giese, and W. R. Gentry, "Sub-miniature ExB sector-field mass spectrometer," *J. Amer. Soc. Mass Spectrom.*, vol. 12, no. 6, pp. 619–632, Jun. 2001.
- [22] S. A. Lammert, A. A. Rockwood, M. Wang, M. L. Lee, E. D. Lee, S. E. Tolley, J. R. Oliphant, J. L. Jones, and R. W. Waite, "Miniature toroidal radio frequency ion trap mass analyzer," *J. Amer. Soc. Mass Spectrom.*, vol. 17, no. 7, pp. 916–922, Jul. 2006.
- [23] D. E. Austin, M. Wang, S. E. Tolley, J. D. Maas, A. R. Hawkins, A. L. Rockwood, H. D. Tolley, E. D. Lee, and M. L. Lee, "Halo ion trap mass spectrometer," *Anal. Chem.*, vol. 79, no. 7, pp. 2927–2932, Apr. 2007.
- [24] D. E. Austin, Y. Peng, B. J. Hansen, I. W. Miller, A. L. Rockwood, A. R. Hawkins, and S. E. Tolley, "Novel ion traps using planar resistive electrodes: Implications for miniaturized mass analyzers," *J. Amer. Soc. Mass Spectrom.*, vol. 19, no. 10, pp. 1435–1441, Oct. 2008.
- [25] Z. Ouyang, G. Wu, Y. Song, H. Li, W. R. Plass, and R. G. Cooks, "Rectilinear ion trap: Concepts, calculations, and analytical performance of a new mass analyzer," *Anal. Chem.*, vol. 76, no. 16, pp. 4595–4605, Aug. 2004.
- [26] Y. Song, G. Wu, Q. Song, R. G. Cooks, Z. Ouyang, and W. R. Plass, "Novel linear ion trap mass analyzer composed of four planar electrodes," *J. Amer. Soc. Mass Spectrom.*, vol. 17, no. 4, pp. 631–639, Apr. 2006.
- [27] L. Gao, Q. Song, G. E. Patterson, R. G. Cooks, and Z. Ouyang, "Handheld rectilinear ion trap mass spectrometer," *Anal. Chem.*, vol. 78, no. 17, pp. 5994–6002, Sep. 2006.
- [28] L. Gao, A. Sugiarto, J. D. Harper, R. G. Cooks, and Z. Ouyang, "Design and characterization of a multisource hand-held tandem mass spectrometer," *Anal. Chem.*, vol. 80, no. 19, pp. 7198–7205, 2008.
- [29] J. A. Contreras, J. A. Murray, S. E. Tolley, J. L. Oliphant, H. D. Tolley, S. A. Lammert, E. D. Lee, D. W. Later, and M. L. Lee, "Hand-portable gas chromatograph-toroidal ion trap mass spectrometer (GC-TMS) for detection of hazardous compounds," *J. Amer. Soc. Mass Spectrom.*, vol. 19, no. 10, pp. 1425–1434, Oct. 2008.
- [30] M. Yang, T.-Y. Kim, H.-C. Hwang, S.-K. Yi, and D.-H. Kim, "Development of a palm portable mass spectrometer," *J. Amer. Soc. Mass Spectrom.*, vol. 19, no. 10, pp. 1442–1448, Oct. 2008.
- [31] C. B. Freidhoff, R. M. Young, S. Sriram, T. T. Braggins, T. W. O'Keefe, J. D. Adam, H. C. Nathanson, R. R. A. Syms, T. J. Tate, M. M. Ahmad, S. Taylor, and J. Tunstall, "Chemical sensing using nonoptical microelectromechanical systems," *J. Vac. Sci. Technol. A, Vac. Surf. Films*, vol. 17, no. 4, pp. 2300–2307, Jul. 1999.
- [32] R. R. A. Syms, "Advances in microfabricated mass spectrometers," *Anal. Bioanal. Chem.*, vol. 393, no. 2, pp. 427–429, Jan. 2009.
- [33] H. J. Yoon, S. H. Song, N. T. Hong, K. W. Jung, S. Lee, and S. S. Yang, "Fabrication of two types of micro ion sources for a micro time-of-flight mass spectrometer," *J. Micromech. Microeng.*, vol. 17, no. 8, pp. 1542–1548, Aug. 2007.
- [34] L. F. Velásquez-García, B. Gassend, and A. I. Akinwande, "CNT-based gas ionizers with integrated MEMS gate for portable mass spectrometry," in *Tech. Dig. Transducers*, Denver, CO, Jun. 2009, pp. 1646–1649.
- [35] P. S. Riehl, K. L. Scott, R. S. Muller, R. T. Howe, and J. A. Yasaitis, "Electrostatic charge and field sensors based on micromechanical resonators," *J. Microelectromech. Syst.*, vol. 12, no. 5, pp. 577–589, Oct. 2003.
- [36] Y. Zhu, J. Lee, and A. Seshia, "System-level simulation of a micro-machined electrometer using a time-domain variable capacitor circuit model," *J. Micromech. Microeng.*, vol. 17, no. 5, pp. 1059–1065, May 2007.
- [37] N. Sillon and R. Baptist, "Micromachined mass spectrometer," *Sens. Actuators B, Chem.*, vol. 83, no. 1–3, pp. 129–137, Mar. 2002.
- [38] H. J. Yoon, J. H. Kim, E. S. Choi, S. S. Yang, and K. W. Jung, "Fabrication of a novel micro time-of-flight mass spectrometer," *Sens. Actuators A, Phys.*, vol. 97/98, pp. 441–447, Apr. 2002.
- [39] E. Wapellhorst, J.-P. Hauschild, and J. Müller, "Complex MEMS: A fully integrated TOF micro mass spectrometer," *Sens. Actuators A, Phys.*, vol. 138, no. 1, pp. 22–27, Jul. 2007.
- [40] S. Pau, C. S. Pai, Y. L. Low, J. Moxom, P. T. Reilly, W. B. Whitten, and J. M. Ramsey, "Microfabricated quadrupole ion trap for mass spectrometer applications," *Phys. Rev. Lett.*, vol. 96, no. 12, pp. 120 801–1–120 801–4, Mar. 2006.
- [41] M. G. Blain, L. S. Riter, D. Cruz, D. E. Austin, G. Wu, W. R. Plass, and R. G. Cooks, "Towards the hand-help mass spectrometer: Design considerations, simulation, and fabrication of micrometer-scaled

- cylindrical ion traps," *Int. J. Mass Spectrom.*, vol. 236, no. 1–3, pp. 91–104, Aug. 2004.
- [42] A. Chaudhary, F. H. W. van Amerom, and R. T. Short, "Development of microfabricated cylindrical ion trap mass spectrometer arrays," *J. Microelectromech. Syst.*, vol. 18, no. 2, pp. 442–448, Apr. 2009.
- [43] R. A. Miller, E. G. Nazarov, G. A. Eiceman, and A. T. King, "A MEMS radio-frequency ion mobility spectrometer for chemical vapor detection," *Sens. Actuators A, Phys.*, vol. 91, no. 3, pp. 301–312, Jul. 2001.
- [44] A. B. Kanu, P. Dwivedi, M. Tam, L. Matz, and H. H. Hill, Jr., "Ion mobility-mass spectrometry," *J. Mass Spectrom.*, vol. 43, no. 1, pp. 1–22, Jan. 2008.
- [45] P. Siebert, G. Petzold, A. Hellenbart, and J. Müller, "Surface microstructure/miniature mass spectrometer: Processing and applications," *Appl. Phys. A, Solids Surf.*, vol. 67, no. 2, pp. 155–160, 1998.
- [46] J.-P. Hauschild, E. Wapelhorst, and J. Müller, "Mass spectra measured by a fully integrated MEMS mass spectrometer," *Int. J. Mass Spectrom.*, vol. 264, no. 1, pp. 53–60, Jun. 2007.
- [47] J. H. Batey, "Quadrupole gas analyzers," *Vacuum*, vol. 37, no. 8/9, pp. 659–668, 1987.
- [48] P. H. Dawson, *Quadrupole Mass Spectrometry and Its Applications*. New York: Amer. Inst. Phys., 1995.
- [49] R. R. A. Syms, T. J. Tate, M. M. Ahmad, and S. Taylor, "Design of a microengineered electrostatic quadrupole lens," *IEEE Trans. Electron Devices*, vol. 45, no. 11, pp. 2304–2311, Nov. 1998.
- [50] S. Taylor, R. F. Tindall, and R. R. A. Syms, "Silicon based quadrupole mass spectrometry using microelectromechanical systems," *J. Vac. Sci. Technol. B, Microelectron. Process. Phenom.*, vol. 19, no. 2, pp. 557–562, Mar. 2001.
- [51] M. Gear, R. R. A. Syms, S. Wright, and A. S. Holmes, "Monolithic MEMS quadrupole mass spectrometers by deep silicon etching," *J. Microelectromech. Syst.*, vol. 14, no. 5, pp. 1156–1166, Oct. 2005.
- [52] S. Wright, R. R. A. Syms, S. O'Prey, G. Hong, and A. S. Holmes, "Comparison of ion coupling strategies for a microengineered quadrupole mass filter," *J. Amer. Soc. Mass Spectrom.*, vol. 20, no. 1, pp. 146–156, Jan. 2009.
- [53] L. F. Velásquez-García, K. Cheung, and A. I. Akinwande, "An application of 3-D MEMS packaging: Out-of-plane quadrupole mass filters," *J. Microelectromech. Syst.*, vol. 17, no. 6, pp. 1430–1438, Dec. 2008.
- [54] D. Wiberg, N. V. Myung, B. Eyre, K. Shcheglov, O. Orient, E. Moore, and P. Munz, "LIGA fabricated two-dimensional quadrupole array and scroll pump for miniature gas chromatography/mass spectrometer," *Proc. SPIE*, vol. 4878, pp. 8–13, 2003.
- [55] S. H. Deshmukh, L. B. King, and C. R. Monroe, "A microscale quadrupole mass spectrometer for ion species analysis," in *Proc. 40th AIAA*, 2004, pp. 1–9.
- [56] D. J. Douglas, T. A. Glebova, N. V. Kononkov, and M. Y. Sudakov, "Spatial harmonics of the field in a quadrupole mass filter with circular electrodes," *Tech. Phys.*, vol. 44, no. 10, pp. 1215–1219, Oct. 1999.
- [57] P. H. Dawson and Y. Bingqi, "The second stability region of the quadrupole mass filter—Part 1: Ion optical properties," *Int. J. Mass Spectrom. Ion Processes*, vol. 56, no. 1, pp. 25–39, Feb. 1984.
- [58] Z. Du, D. J. Douglas, and N. Kononkov, "Elemental analysis with quadrupole mass filters operated in higher stability regions," *J. Anal. Atomic Spectrom.*, vol. 14, no. 8, pp. 1111–1119, 1994.
- [59] N. V. Kononkov and J. T. Dowell, "Transmission of the quadrupole mass filter in the intermediate stability zone separation mode," *Int. J. Mass Spectrom. Ion Processes*, vol. 164, no. 3, pp. 201–206, Oct. 1997.
- [60] S. Hiroki, T. Abe, and Y. Murakami, "Development of a quadrupole mass spectrometer using the second stable zone in Mathieu's stability diagram," *Rev. Sci. Instrum.*, vol. 62, no. 9, pp. 2121–2124, Sep. 1991.
- [61] P. Turner, S. Taylor, and J. R. Gibson, "Effect of ion entry acceptance conditions on the performance of a quadrupole mass spectrometer operated in upper and lower stability regions," *J. Vac. Sci. Technol. A, Vac. Surf. Films*, vol. 23, no. 3, pp. 480–487, May 2005.
- [62] Z. Du, D. J. Douglas, T. Glebova, and N. V. Kononkov, "Peak structure with a quadrupole mass filter operated in the third stability region," *Int. J. Mass Spectrom.*, vol. 197, no. 1–3, pp. 113–121, Feb. 2000.
- [63] K. Cheung, L. F. Velásquez-García, and A. I. Akinwande, "Fully batch-fabricated linear quadrupole mass filters," in *Tech. Dig. Hilton Head*, 2008, pp. 316–319.
- [64] P. H. Dawson, "Fringing fields in quadrupole-type mass analyzers," *J. Vac. Sci. Technol.*, vol. 9, no. 1, pp. 487–491, Jan. 1971.
- [65] T. J. Hogan, S. Taylor, K. Cheung, L. F. Velásquez-García, A. I. Akinwande, and R. E. Pedder, "Performance characteristics of a MEMS quadrupole mass filter with square electrodes—Experimental and simulated results," *IEEE Trans. Instrum. Meas.*, to be published.
- [66] D. J. Douglas and N. V. Kononkov, "Influence of the 6th and 10th spatial harmonics on the peak shape of a quadrupole mass filter with round rods," *Rapid Commun. Mass Spectrom.*, vol. 16, no. 5, pp. 1425–1431, Aug. 2002.
- [67] J. R. Gibson and S. Taylor, "Asymmetrical features of mass spectral peaks produced by quadrupole mass filters," *Rapid Commun. Mass Spectrom.*, vol. 17, no. 10, pp. 1051–1055, May 2003.
- [68] R. R. A. Syms, L. Michelutti, and M. M. Ahma, "Two-dimensional micro-fabricated electrostatic Einzel lens," *Sens. Actuators A, Phys.*, vol. 107, no. 7, pp. 285–295, Nov. 2003.
- [69] P. H. Dawson, "The acceptance of the quadrupole mass filter," *Int. J. Mass Spectrom. Ion Phys.*, vol. 17, no. 4, pp. 423–445, Aug. 1975.
- [70] D. J. Douglas and N. V. Kononkov, "Ion source emittance influence on the transmission of a quadrupole operated in the second stability region," *J. Amer. Soc. Mass Spectrom.*, vol. 9, no. 10, pp. 1074–1080, Oct. 1998.
- [71] V. V. Titov, "Detailed study of the quadrupole mass analyzer operating within the first, second, and third (intermediate) stability regions—Part 2: Transmission and resolution," *J. Amer. Soc. Mass Spectrom.*, vol. 9, no. 1, pp. 70–87, 1998.
- [72] J. R. Gibson, S. Taylor, and J. H. Leck, "Detailed simulation of mass spectra for quadrupole mass spectrometer systems," *J. Vac. Sci. Technol. A, Vac. Surf. Films*, vol. 18, no. 1, pp. 237–243, Jan. 2000.
- [73] T. J. Hogan and S. Taylor, "Performance simulation of a quadrupole mass filter operating in the first and third stability zones," *IEEE Trans. Instrum. Meas.*, vol. 57, no. 3, pp. 498–508, Mar. 2008.
- [74] C. S. Trajber, M. Simon, and M. Csontos, "On the use of pre-filters in quadrupole mass spectrometers," *Meas. Sci. Technol.*, vol. 2, no. 8, pp. 785–787, Aug. 1991.
- [75] S. Hiroki, K. Sakata, N. Sugiyama, S. Muramoto, T. Abe, and Y. Murakami, "Effects of a pre-filter on the sensitivity of a high-resolution quadrupole mass spectrometer," *Vacuum*, vol. 46, no. 7, pp. 681–683, Jul. 1995.
- [76] Z. Du and D. J. Douglas, "A novel tandem quadrupole mass analyzer," *J. Amer. Soc. Mass Spectrom.*, vol. 10, no. 11, pp. 1053–1066, Nov. 1999.



**Kerry Cheung** (M'09) received the B.S. degree (*magna cum laude*) in applied and engineering physics from Cornell University, Ithaca, NY, in 2003, and the M.S. and Ph.D. degrees in electrical engineering from the Massachusetts Institute of Technology (MIT), Cambridge, MA, in 2005 and 2009, respectively.

He is currently a Postdoctoral Associate with the Microsystems Technology Laboratories, MIT, continuing his work on portable mass spectrometry and exploring microarrayed electrospraying. He is the author of two journal publications and six conference proceedings entries. He is the holder of two pending patents on MEMS mass analyzers. His research interests include the application of microfabrication and nanofabrication technologies for MEMS/NEMS sensor development, integrated microsystems, instrument miniaturization, biotechnology, and renewable energy.



**Luis Fernando Velásquez-García** (M'09) received the Mechanical Engineer degree (*magna cum laude*) and valedictorian of the School of Engineering and the Civil Engineer degree (*magna cum laude* and valedictorian of the School of Engineering) from the Universidad de Los Andes, Bogotá, Colombia, in 1998 and 1999, respectively, and the M.S. and Ph.D. degrees from the Department of Aeronautics and Astronautics, Massachusetts Institute of Technology (MIT), Cambridge, in 2001 and 2004, respectively.

In 2004, after completing his studies, he became a Postdoctoral Associate in the Microsystems Technology Laboratories (MTL), MIT, where he was appointed as a Research Scientist in 2005. Since 2009, he has been a Principal Scientist and Core Member with MTL. He is an expert in micro- and nanofabrication technologies, and his research focuses on the application of micro- and nanotechnology to multiplexed scaled-down systems to attain better performance. He has conducted research in micro- and nanotechnologies applied to electrospray, carbon-nanotube-based devices, 3-D packaging, mass spectrometry, propulsion, and chemical reactors. He has authored more than 15 journal publications and 30 conference proceedings entries. He is the holder of six patents on MEMS technologies.

Dr. Velásquez-García is a full member of Sigma Xi and a senior member of the American Institute of Aeronautics and Astronautics (AIAA).





**Akintunde Ibitayo (Tayo) Akinwande** (S'81–M'86–SM'04–F'08) received the B.Sc. degree in electrical and electronic engineering from the University of Ife, Ife, Nigeria, in 1978, and the M.S. and Ph.D. degrees in electrical engineering from Stanford University, Stanford, CA, in 1981 and 1986, respectively.

In 1986, he joined Honeywell International, Inc., Morristown, NJ, where he initially conducted research on GaAs complementary FET technology for very-high-speed and low-power signal processing.

He later joined the Si Microstructures Group, where he conducted research on pressure sensors, accelerometers, and thin-film field emission and display devices. In January 1995, he joined the Microsystems Technology Laboratories, Massachusetts Institute of Technology (MIT), Cambridge, where his research focuses on microfabrication and electronic devices, with particular emphasis on smart sensors and actuators, intelligent displays, large-area electronics (macroelectronics), field-emission and field-ionization devices, mass spectrometry, and electric propulsion. He was a Visiting Professor in the Department of Engineering and an Overseas Fellow at Churchill College, Cambridge University, Cambridge, U.K., in 2002 and 2003. He is currently a Professor in the Department of Electrical Engineering and Computer Science, MIT. Since September 2009, he has been the Program Manager of the Microsystems Technology Office, Defense Advanced Research Projects Agency. He is the author of more than 100 journal publications and is the holder of numerous patents in the areas of MEMS, electronics on flexible substrates, and display technologies.

Prof. Akinwande was the recipient of a 1996 National Science Foundation CAREER Award. He is currently a member of the IEEE Nanotechnology Council. He has served on a number of Technical Program Committees for various conferences, including the Device Research Conference, the IEEE International Electron Devices Meeting, the IEEE International Solid-State Circuits Conference, the International Display Research Conference, and the International Vacuum Microelectronics Conference.